Oxidation behavior and mechanical properties of a directionally solidified high Nb TiAl based alloy between 800 °C and 900 °C

Xuesong Xu [a], He Liang [b], Hongsheng Ding [b], Karl P. Davidson [c], R.V. Ramanujan [c], Ruirun Chen [b], Jingjie Guo [b], Hengzhi Fu [b]

[a] School of Materials Science and Engineering, Nanjing University of Science and Technology, Nanjing, 210094, China

[b] School of Materials Science and Engineering, Harbin Institute of Technology, Harbin, 150001, China

[c] School of Materials Science and Engineering, Nanyang Technological University, 50 Nanyang Avenue, Singapore, 639798, Singapore

Abstract

The high temperature oxidation behavior and mechanical property response of a directionally solidified Ti-46Al-7Nb-0.4W-0.6Cr-0.1B alloy were investigated. The ultimate tensile strength of the alloy at 800 °C, 850 °C and 900 °C are 647 MPa, 590 MPa and 508 MPa, respectively, and the tensile fracture mode changed from brittle cleavage fracture to micro-void accumulation ductile fracture. At lower temperatures Al_2O_3 forms first, growing along the γ lamellae to form oxide bands aligned with the lamellar orientation. The oxidation mass gain of the alloy after 900 °C/100 h isothermal oxidation is only 0.91 mg/cm^2. The oxidation kinetics results show the microalloyed high Nb TiAl alloy has excellent oxidation resistance, which is due to the formation of a TiO_2 layer containing Nb, Cr and W, the $AlNb_2$ phase and an Al/Cr rich transition layer above the directionally solidified lamellar matrix.

Keywords

High Nb TiAl alloy

Mechanical property

Directional solidification

Oxidation behavior

1. Introduction

TiAl based alloys have wide application potential in the aerospace and automotive energy fields because of their low density, high specific strength, good creep and fatigue resistance [[1], [2], [3]]. Compared with traditional 2nd generation TiAl based alloys, TiAl based alloys with high Nb content have superior high temperature performance [[4], [5], [6], [7], [8]]. However, their poor ductility at room temperature and limited hot working ability are challenges to the fabrication and processing of these alloys. One method that can be successful in processing high Nb TiAl alloys is directional solidification technology [9]. Directional solidification can eliminate transverse grain boundaries and provide directional columnar crystals or even single crystals, which can greatly improve the high temperature performance of high Nb TiAl based alloys with directional lamellar microstructures. To increase the service temperatures of TiAl based alloys, the high temperature mechanical properties and oxidation resistance must be considered [10]. Zhang et al. [11] tested the high temperature tensile properties of high Nb TiAl and found that the brittle-ductile transition temperature of the alloy was between 880 °C and 920 °C; the dynamic recrystallization during the deformation process at high temperatures promoted plastic deformation. Liu et al. [12] noted that the main softening mechanisms of high Nb TiAl alloys deformed at 800 °C and 1000 °C were phase transformations and dynamic

recrystallization, respectively.

The properties of TiAl alloys also change at elevated temperatures, influencing the diffusion rate, the fracture mode and the phase transformation process [13]. The cavity formation process of a high Nb TiAl alloy during high temperature tensile testing was studied by Zhu et al. [14]. The cavitation of the alloy is dominated by diffusion-controlled cavity nucleation; the higher the temperature, the greater the cavity nucleation. The temperature dependence of the fatigue crack growth properties was studied by Sakaguchi et al. [15], the temperature-dependent fatigue threshold was related to the crack closure mechanism induced by roughness related oxidation. Furthermore, the effect of temperature on the tensile properties was studied by Hashimoto et al. [16], with the authors observing an elongation increase with rising temperature due to the reduction of environmental brittleness and an increase in the occurrence of twinning. The mechanical properties and the fracture behavior of a directionally solidified Ti-47Al-2Cr-2Nb alloy across a range of temperatures up to 900 °C was evaluated by Wang et al. [17], it was found that the toughening mechanism at medium and low temperatures were small plastic deformation and increasing crack surface energy, respectively. As seen by these works, there is a wealth of knowledge on the high temperature property response of binary TiAl based alloys however, the temperature dependent high temperature tensile behavior of high Nb TiAl based alloys with a directionally solidified microstructure is still unclear.

The high temperature oxidation resistance of traditional TiAl alloys is inadequate above 800 °C as they are unable to form a dense protective Al_2O_3 film layer, with the rapid growth of the TiO_2 layer insufficient for long-term oxidation protection. To further improve the oxidation resistance, many researchers enhance the oxidation resistance of TiAl based alloys by adding alloying elements, such as Nb [[18], [19], [20]], Cr [21], Mo [22], W [23], Ta [24], Y [25], Si [26], Sn [27] and B [28], etc. One of the most effective alloying elements is Nb, as it has a higher chemical valency than Ti. Due to the electric neutrality of the oxide, the concentration of oxygen vacancies can be reduced by the presence of Nb, restricting internal oxidation and inhibiting the growth of TiO_2 [29]. Nb can also increase the thermodynamic activity of Al relative to that of Ti, promoting the formation of a more stable Al_2O_3 layer [30], and facilitating the formation of TiN layers at the interface between the oxide and the matrix, preventing the diffusion of Ti and O [19]. The oxidation resistance of TiAl alloy varies with temperature, which determines the application temperature range the alloy. The oxidation behavior of two TiAl compositions containing the β_o phase was conducted by Mengis et al. [31]. Testing was conducted between 600 and 900 °C with the $\beta_o \rightarrow \alpha_2$ phase transformation in this temperature window resulting in an increase in oxygen content in the subsurface region, which is detrimental to the mechanical properties of the alloys. The oxidation behavior of TiAl alloys, containing various alloying elements, between 800 and 1000 °C was studied by Shida et al. [31]. They concluded from oxidation studies that the mass gain of a TiAl alloyed with Mo tested at 900 °C and a W alloyed TiAl tested at 1000 °C was comparable to that of a Ti-48.6Al alloy at 800 °C, highlighting the improved resistance with alloying. Microalloying addition of W between 0 and 1 at% to the commercial Ti-48Al-2Cr-2Nb alloys was studied by Seo et al. [23] at temperatures between 800 and 1000 °C. It was reported that the W element addition reduced the oxidation rate and the sensitivity of the oxidation rate to temperature. The kinetics of oxidation of a TiAl alloy was studied by Taniguchi et al. [32] in a pure oxygen environment at temperatures between 727 and 1127 °C. The oxidation kinetics followed an approximately linear rate in the initial stage of oxidation, followed by a gradual decrease in the oxidation rate with time. A similar linear relationship in oxidation at 750 °C was reported by Wang et al. [33] for an in-situ autogenous Ti_2AlC phase TiAl alloy, changing to a cubic relationship at 850 °C. The

studies on the oxidation behavior of TiAl alloys with respect to temperature are mostly focused on 2nd generation TiAl alloys. However, the oxidation mechanism and kinetics behavior of high Nb TiAl with temperature has been much less investigated and is worthy of further study.

Therefore, the purpose of this study is to reveal the effect of temperature on the high temperature mechanical properties and oxidation resistance of a directionally solidified (DS) high Nb TiAl based alloy. The high Nb TiAl alloy with minor W, Cr and B addition was prepared by a cold crucible directional solidification technique. The high temperature tensile properties were tested, and isothermal oxidation experiments were carried out to evaluate the oxidation resistance of the alloy at temperatures between 800 °C and 900 °C. Finally, the oxidation kinetics and crystallographic related oxidation mechanism of oxidation of DS high Nb TiAl alloy is discussed.

2. Materials and methods

2.1. Materials preparation

A microalloyed high-Nb TiAl master alloy was investigated in this study, with a nominal composition of Ti-46Al-7Nb-0.4W-0.6Cr-0.1B (at. %). The master ingot was prepared by vacuum consumable melting and induction skull melting. Round bars with a diameter of 20 mm were cut from the master alloy by wire electrical discharge machining (EDM), and further processed by electromagnetic cold crucible directional solidification (CCDS), which was carried out under a high purity argon atmosphere with a power of 45 kW and a pulling rate of 8.3 μm/s. The steps and methods of CCDS are reported in prior work [[34], [35], [36]]. Finally, a DS square ingot with a size of 30 × 30 × 120 mm was obtained.

2.2. Tensile test

The CCDS ingots were cut into high temperature tensile test specimens with a cross-section of 5 × 2 mm and a gauge length of 15 mm. To obtain adequate surface finish and eliminate stress concentration caused by surface defects, the specimen surfaces, especially the two end faces, were subjected to grinding by SiC abrasive papers with reducing grit size down to 3000#. The axial high temperature tensile tests were performed in an Electronic Universal Material Testing Machine (AG-X plus250 kN, Shimadzu Corporation, Japan), with a strain rate of $5 \times 10^{-4}\ s^{-1}$, at 800 °C, 850 °C and 900 °C, respectively. A minimum of three tests were performed for each condition and average values reported. The tested sample is contained inside a resistance furnace, with temperature measurements collected at the top, middle and bottom of the resistance furnace. The tensile test procedure commences after a dwell of 15 min, to ensure stability in the preset temperatures between all three measuring devices.

2.3. Oxidation test

Samples for the oxidation test were cut from the DS ingot to a size of 10 × 10 × 2 mm. Before oxidation, the samples were mechanically ground by SiC abrasive papers from 400# to 3000#, and polished to remove scratches on the surface for subsequent microstructural observation. Isothermal oxidation experiments were conducted in a box heat treatment furnace at 800, 850 and 900 °C in air. Each sample was placed in a separate corundum crucible and covered by a corundum slip with small holes to prevent the spalled oxide scale from exiting the crucible and to ensure adequate contact between the samples and air.

2.4. Microstructure characterization

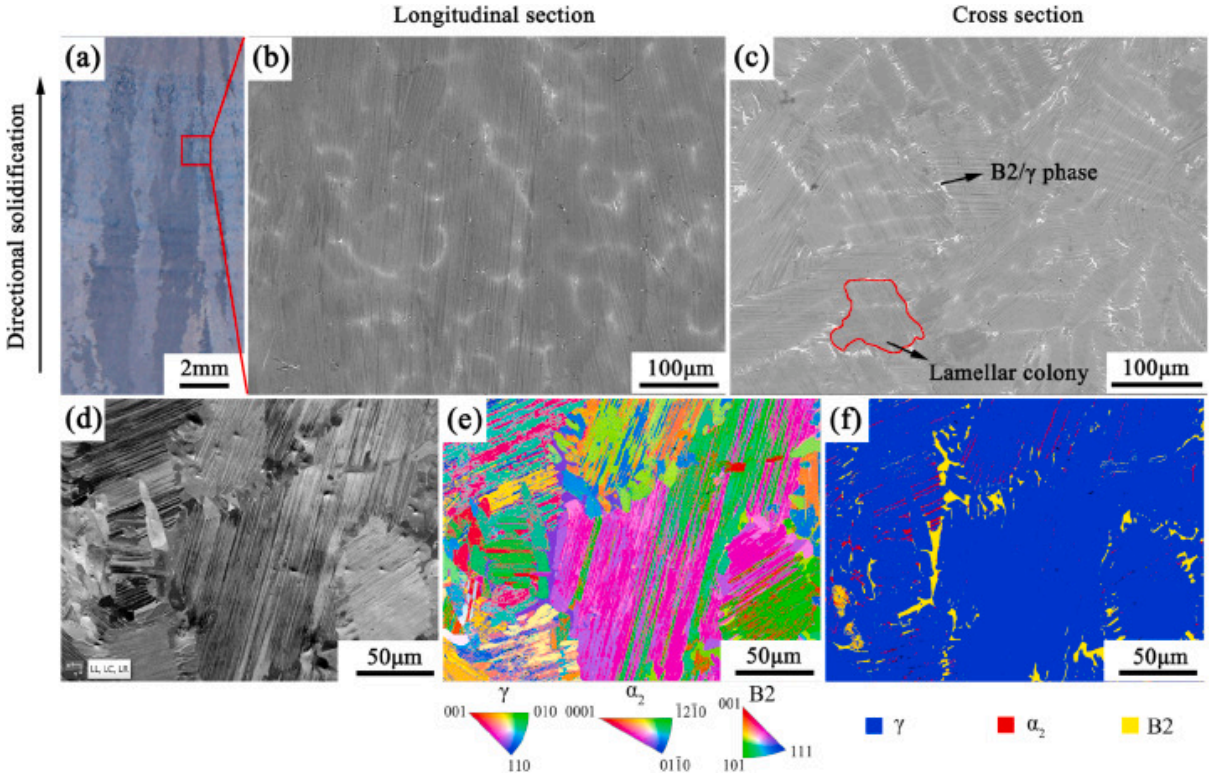
Samples used for microstructure characterization were first ground with SiC abrasive papers to 3000#, then polished. The DS samples were cut from the middle of the ingot and prepared using standard metallography techniques before etching in a modified Kroll reagent containing 5 vol% HF, 10 vol%

HNO_3 and 85 vol% H_2O. Macrostructures were obtained on a Nikon D850 Digital Single Lens Reflex camera. Microstructural observations were conducted on a JEOL FESEM 7800F scanning electron microscope (SEM) with energy dispersive spectroscopy (EDS) and electron backscattered diffraction (EBSD) techniques. The same SEM was used in the secondary electron (SE) mode to image the fracture morphology of the tested samples. Phase constituents of the samples were examined by a Bruker D2 X-ray diffraction (XRD) utilizing a Cu Kα radiation source. Samples were scanned in the 2θ range of 20~90° at a speed of 0.85°min^{-1}.

3. Results

3.1. Macro/microstructure of DS high TiAl alloy

The macro- and microstructure of the DS high Nb TiAl based alloy are presented in Fig. 1 with the columnar crystal shown in Fig. 1(a), showing a DS direction from the bottom of the image to the top, the growth of the crystals is parallel to the DS direction. The high magnification SEM image of the longitudinal section microstructure, evident in the red wire frame region of Fig. 1(a), is presented in Fig. 1(b). The microstructure comprises of α_2/γ lamellae, bright white segregation bands, and dispersed boride precipitates inside the lamellae colony. Lamellar colonies form parallel to the DS direction, the lamellar orientation in a single lamellar colony is uniform. The angle between the adjacent lamellar colony and the DS direction is less than 10°. The cross-sectional micrograph of the DS sample is presented in Fig. 1(c). The corresponding forescatter detector (FSD), grain texture maps and phase distribution maps are presented in Fig. 1(d), (e) and (f) respectively. The lamellar growth direction is random, as seen in the microstructural cross-section. White Nb segregation bands exist inside the lamellar colony. Structures composed of bright B2 and blocky γ phase between the lamellar colonies were also observed.



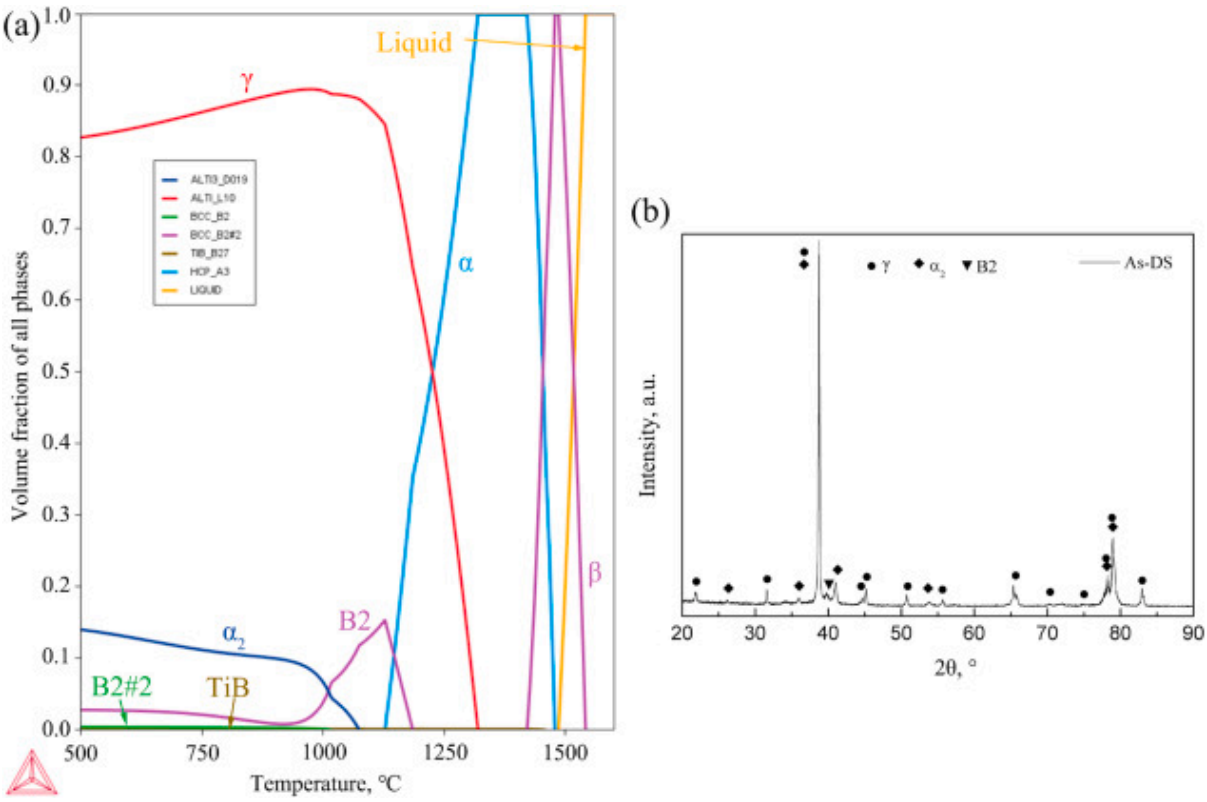
1. Download: Download high-res image (2MB)
2. Download: Download full-size image

Fig. 1. Macro- and microstructure of DS high Nb TiAl alloy. (a) Parallel columnar crystal, (b)

Longitudinal section microstructure, (c) Cross section microstructure, (d) FSD images, (e) grain texture maps and inverse pole figures (IPF), (f) Phase distribution maps.

3.2. Constituent phases

The volume fraction of each phase in the equilibrium phase diagram of the alloy, as calculated by Thermo-calc, is presented in Fig. 2(a). The low-temperature phases include the α_2-Ti_3Al ($D0_{19}$), γ-TiAl ($L1_0$), B2 and TiB (B27) phases, with the corresponding volume fractions; γ phase 82.8 %, α_2 phase 14.0 %, B2 phase 2.8 % and, TiB phase 0.4 %. Based on the calculated phase diagram, the α phase stability ranges from 1317–1422 °C, the α phase completely dissolves at 1128 °C. There is a gap of 54 °C between the α phase region and the α_2 phase region, with the α_2 phase appearing from 1074 °C. The B2 phase formation begins at 1184 °C, gradually increasing in content to 1128 °C, and then decreases in content with the increase of α_2 phase (Purple and dark blue lines). The γ phase appears at 1320 °C, it's content gradually increased with lower temperature. Due to the precipitation of the B2 phase, the γ phase content decreased slightly. Furthermore, the TiB phase occurs because of its high melting point. The solidification path follows: L (Liquid) → L+β → α+β → α → α+γ → α+γ+B2 → γ+B2 → γ+B2+α_2. The phases evident at room temperature are denoted in the XRD pattern presented in Fig. 2(b), the γ, α_2 and B2 phases were observed, consistent with the calculated phase diagram in Fig. 2(a) and EBSD results in Fig. 1. Due to the low content of TiB it cannot be detected in the XRD pattern.



1. Download: Download high-res image (396KB)
2. Download: Download full-size image

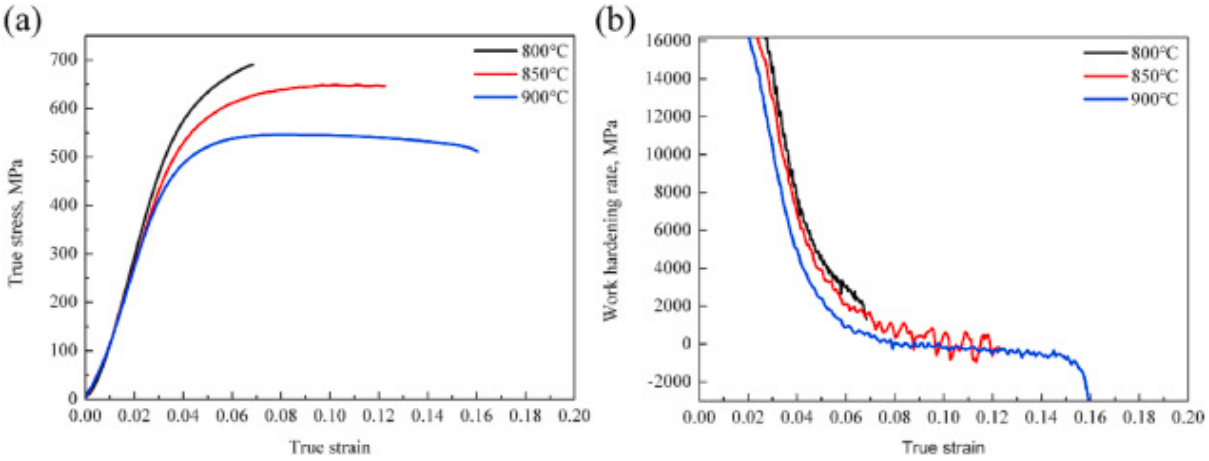
Fig. 2. Constituent phases of the microalloyed high Nb TiAl alloy. (a) Equilibrium phase content diagram of the alloy, (b) XRD pattern.

3.3. High temperature tensile properties

3.3.1. Stress-strain curves of high Nb TiAl based alloy at high temperatures

At the test temperature of 800 °C, the ultimate tensile strength (UTS) and elongation (EL) are 647 MPa

and 3.8 % respectively, decreasing to 590 MPa and 9.5 % at 850 °C. At 850 °C, the alloy shows promising results, the UTS of the alloy is higher than the value for a forged Ti-45Al-8.5Nb-0.2W-0.2B-0.02Y alloy reported by Ding et al. (546 MPa) [4] and the Ti-43Al-6Nb-1Mo-1Cr alloy reported by Li et al. (540 MPa) [37]. The highest test temperature of 900 °C results in a UTS and EL of 508 MPa and 14.9 %, respectively. The high temperature tensile true stress-strain curves at 800, 850 and 900 °C are presented in Fig. 3(a), and the work hardening rate curve of the alloy at each of the test temperatures is presented in Fig. 3(b). The work hardening rate of the high Nb TiAl alloy decreases with increasing test temperature. The work hardening rate can be divided into three stages: (1) rapid decrease in nonlinear work hardening rate with high true strain; (2) slow decrease in work hardening rate with high true strain; (3) Sharp drop in work hardening rate. The first two stages can be found at 800 and 850 °C, while the complete work hardening process at 900 °C. Zheng et al. [38] showed that the work hardening tendency is related to the activation of the twinning system during deformation, the so-called twin-induced plasticity effect.

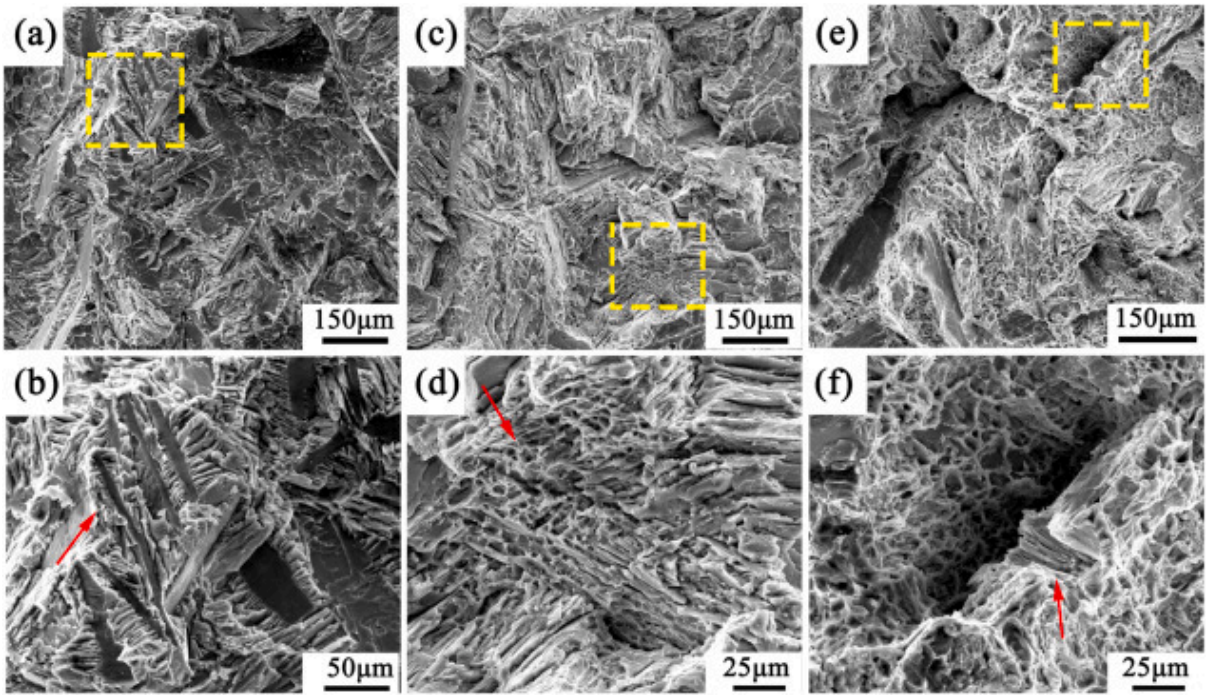


1. Download: Download high-res image (307KB)
2. Download: Download full-size image

Fig. 3. Tensile properties of at 800, 850 and 900 °C. (a) True stress-strain curves, (b) Work hardening curves.

3.3.2. Fracture morphology

SE images of the fracture morphology of samples after tensile tests at 800, 850 and 900 °C are presented in Fig. 4. The trans-lamellar fracture mode is revealed upon observing the fracture surface at all temperatures. This phenomenon occurs because the tensile sample is cut along the DS direction of the ingot. As presented in Fig. 1, the angle between the lamellar orientation and the DS direction is less than 10°, as such the trans-lamellar fracture morphology formed is due to the parallel lamellae being torn. Fig. 4(a) and (b) shows the fracture morphology after the tensile test at 800 °C. The fracture tearing edge is observed which corresponds to the parallel lamellar structure. Furthermore, there are long strips of pits inside the lamellae, which form from the TiB phase. These TiB phases across the lamellae can inhibit interlamellar crack opening and propagation during tensile deformation. As the test temperature increased to 850 °C (Fig. 4(c)), the fracture tearing edge softened and micropores formed (red arrow in Fig. 4(d)), resulting in a fracture morphology with both brittle and plastic characteristics. When tested at 900 °C, the tearing edge completely softened and became blunt. The fracture morphology is characterized by micro-void accumulation based ductile fracture, dominated by dimples (Fig. 4(e) and (f)).



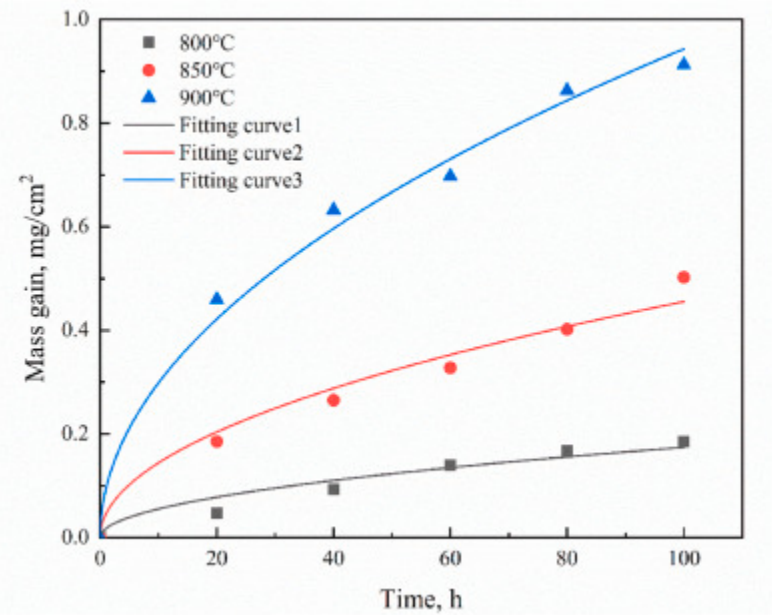
1. Download: Download high-res image (2MB)
2. Download: Download full-size image

Fig. 4. Fracture morphology of DS high Nb TiAl alloy from tensile tested between 800 and 900 °C. (a) and (b) 800 °C, (c) and (d) 850 °C, (e) and (f) 900 °C.

3.4. Isothermal oxidation

3.4.1. Oxidation mass gain curve

The oxidation mass gain results of the DS high Nb TiAl based alloy at 800, 850 and 900 °C for 0–100 h are presented in Fig. 5. An increase in oxidation temperature and time, corresponds to a relative increase in mass gain. The mass gain after 100 h oxidation at 800, 850 and 900 °C was 0.186, 0.502 and 0.912 mg/cm^2, respectively. The relationship between oxidative weight gain and time is as follows:ΔMn=kntWhere, ΔM is the mass gain per unit surface area (mg/cm^2), t is the oxidation time (h), k_n is the oxidation rate constant (mg^n/cm^{2n}/h). According to the fitting results, the oxidation index n is close to 2, and the oxidation reaction rate constant follows the parabolic law and k_p at the three temperatures is 3.03×10^{-4}, 2.07×10^{-3} and 8.89×10^{-3} mg^2/cm^4/h, respectively. This indicates that the oxidation rate increases significantly with higher diffusion rate caused by temperature. The oxidation rate of this alloy is much lower than the commercial Ti-48Al-2Cr-2Nb alloy (1.71×10^{-2}) [33] and Ti-45Al-8Nb (2.85×10^{-3}) [39] at 850 °C, highlighting its great oxidation resistance.

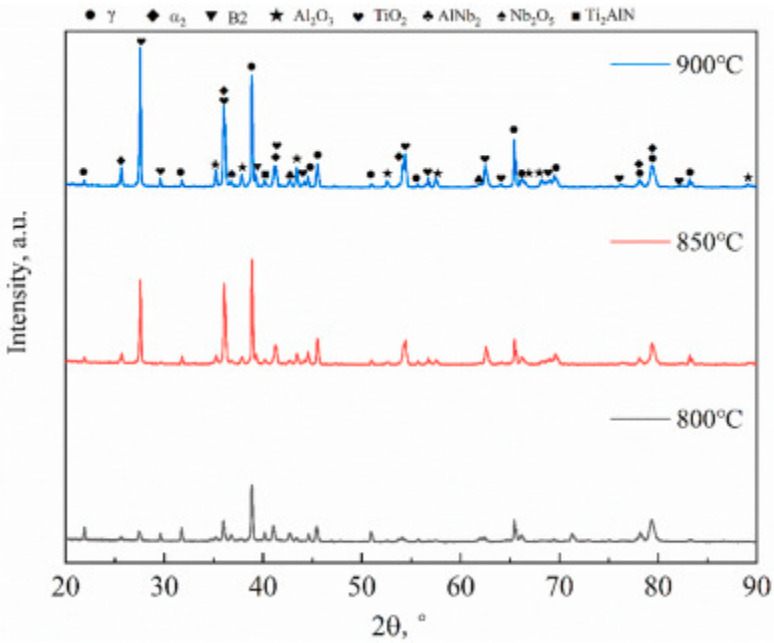


1. Download: Download high-res image (794KB)
2. Download: Download full-size image

Fig. 5. Mass gain and fitting curves for the DS high Nb TiAl alloy at 800, 850 and 900 °C.

3.4.2. XRD pattern after oxidation test

Fig. 6 shows the XRD pattern of DS high Nb TiAl alloy after oxidation for 100 h at 800, 850 and 900 °C. After isothermal oxidation, the constituent γ, α_2 phase and B2 phases are retained. A large amount of Al_2O_3 phase and TiO_2 phase can be detected in all samples, in addition to a small quantity of $AlNb_2$ and Nb_2O_5 phase. With increasing oxidation temperature, the number and intensity of the diffraction peaks of Al_2O_3 and TiO_2 increased significantly, indicating an increase in the oxide layer thickness and the amount of oxidation products. It is worth noting that the peaks of $AlNb_2$ and Nb_2O_5 at 800 °C are small, the diffraction peaks of these two phases can be easily observed at higher temperatures, which indicates that increasing temperature can promote the production of oxidation products containing Nb. The Ti_2AlN phase is also detected as a result of N diffusion through the oxide layer.



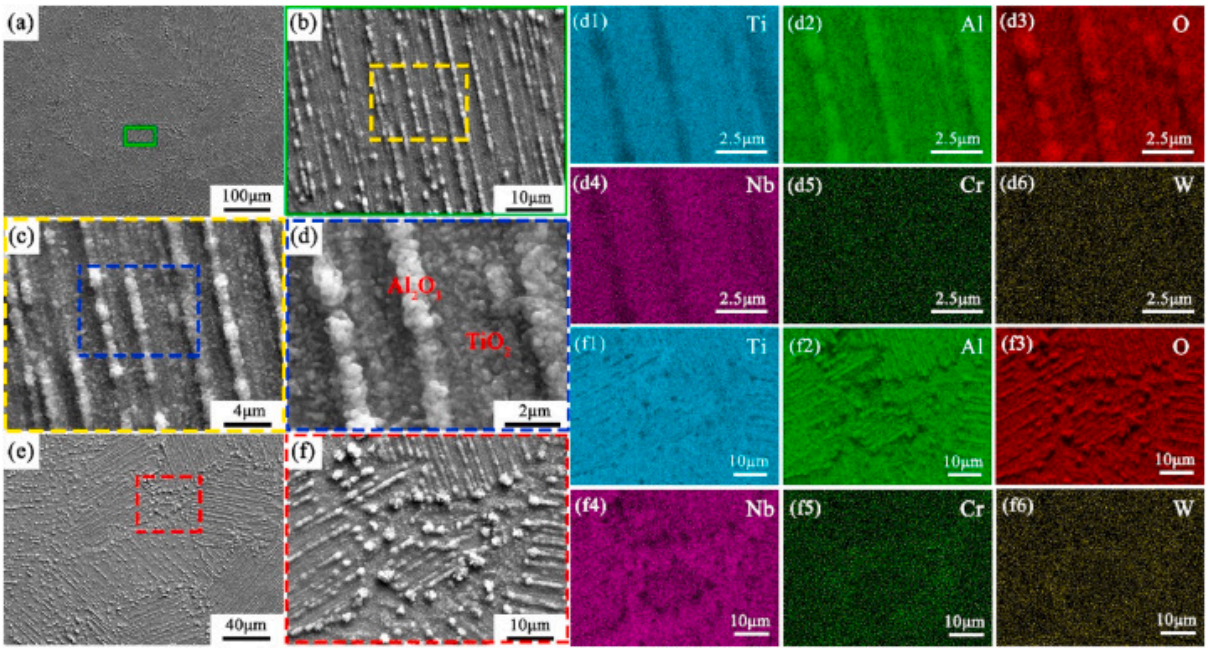
1. Download: Download high-res image (717KB)
2. Download: Download full-size image

Fig. 6. XRD patterns of DS high Nb TiAl alloy after 100 h oxidation tests at 800 °C, 850 °C and 900 °C.

3.4.3. Oxide surface and cross-sectional morphology

3.4.3.1. 800 °C results

Fig. 7 shows the oxide surface morphology of the DS high Nb TiAl alloy after 100 h oxidation at 800 °C. Oxides appear on the surface of the alloy after prolonged oxidation exposure, the oxides are parallel to each other, and lie along the direction of the lamellar structure. Since the observed surface is a cross-section of the DS ingot, there are various arrangements of the oxidation products inside the different colonies, consistent with the lamellar arrangement in each colony, as shown in Fig. 7(a)–(d). This phenomenon shows that the formation of oxide in the lamellar colony is affected by crystallographic factors.



1. Download: Download high-res image (3MB)
2. Download: Download full-size image

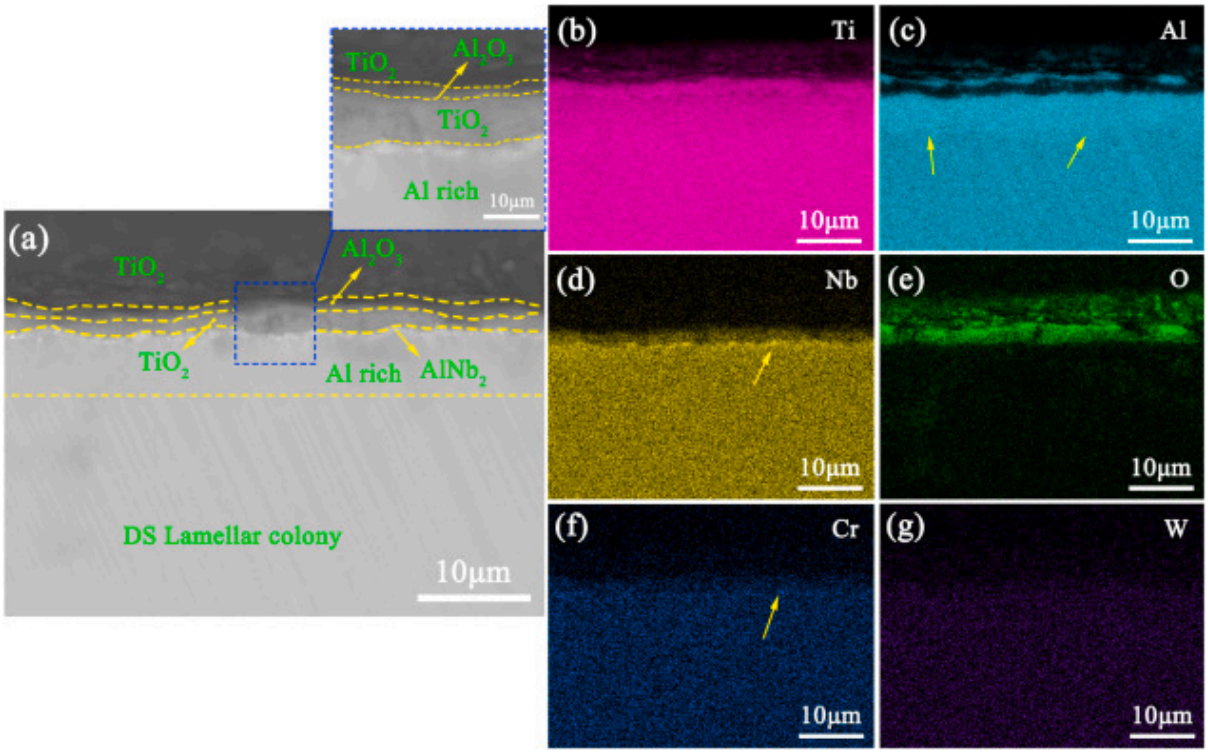
Fig. 7. Microscopic oxidation surface morphology of DS high Nb TiAl alloy after oxidation at 800 °C for 100 h, (a)~(d) lamellar colony, (d1)~(d6) elemental EDS mapping of (d), (e) and (f) junction of lamellar colony, (f1)~(f6) elemental EDS mapping of (f).

Elemental maps of the lamellar colony in Fig. 7(d) are shown in Fig. 7(d1)-(d6). The oxide distributed along the lamellar arrangement direction is rich in Al and O, and lean in Ti and Nb. Combined with the XRD results, it can be inferred that it is the Al_2O_3 phase. In addition, Ti is enriched between the Al_2O_3 phase which is arranged parallel along the lamellar direction. The Ti rich phases are small TiO_2 particles according to the XRD results. These particles are also enriched in Nb and slightly enriched in W and Cr. The presence of these slow-diffusing elements can inhibit oxidation to a certain extent. The arrangement of the oxides along the lamellar orientation is due to the alternating arrangement of the α_2 and γ lamellae within the lamellar colony. Lee et al. [40] pointed out that the Al-rich oxide phase was precipitated in the TiAl plates and the Ti-rich oxide phase in the Ti_3Al plates.

The high magnification image of the boxed section of Fig. 7(e) is presented in Fig. 7(f). This region shows the oxide surface morphology at the junction of four lamellar colonies with different

orientations. The size of the alumina particles at the termination of the lamella is larger than the rest of the lamellae. The elemental distribution diagram was obtained by EDS for this position, as shown in Fig. 7(f1)-(f6). Nb, W and Cr are enriched at the lamellar junction, but the oxides at the lamellar junction are not obvious, indicating that the oxidation resistance of the region rich in these β-stabilizing elements is stronger than that of the lamellar region.

As the elements detected by EDS are from a certain depth within the materials, which may not necessarily be at the visible outer surface. Both top and transverse section view were considered to identified the oxidation layer. The oxide cross-sectional morphology of DS high Nb TiAl alloy after 100 h oxidation at 800 °C is presented in Fig. 8, showing microstructural changes from the surface oxide layer to the matrix. As seen in Fig. 8(a), after oxidation at 800 °C/100 h, the microstructure of the DS high Nb TiAl alloy can be divided into three zones: surface oxide layer, matrix transition zone and internal directional lamellar zone, from the free surface respectively. According to the elemental distribution maps (Fig. 8(b)–(g)), there is minor enrichment of Ti and Al in the upper part of the surface oxide layer, followed by a thin Al rich layer and thick Ti layer below it. Between the oxide layer and the matrix transition zone, there is also a thin Nb rich layer, corresponding to the $AlNb_2$ phase, as seen in the XRD results (Fig. 6). Therefore, the oxide layer from top to bottom at 800 °C is TiO_2+Al_2O_3 layer (thin), Al_2O_3 layer and TiO_2 layer, respectively. There is no evidence of the lamellar structure in the matrix transition zone, where Al is enriched at a thickness of ~6.3 μm. However, Nb and a small content of Cr is enriched at the surface of the matrix transition zone. The α_2/γ layers are arranged in parallel in the matrix as can be seen in the BSE image of Fig. 8(a) and the Al distribution map (Fig. 8(c)). Meanwhile Nb, Cr and W are distributed uniformly in the matrix with no lamellar colony preference.

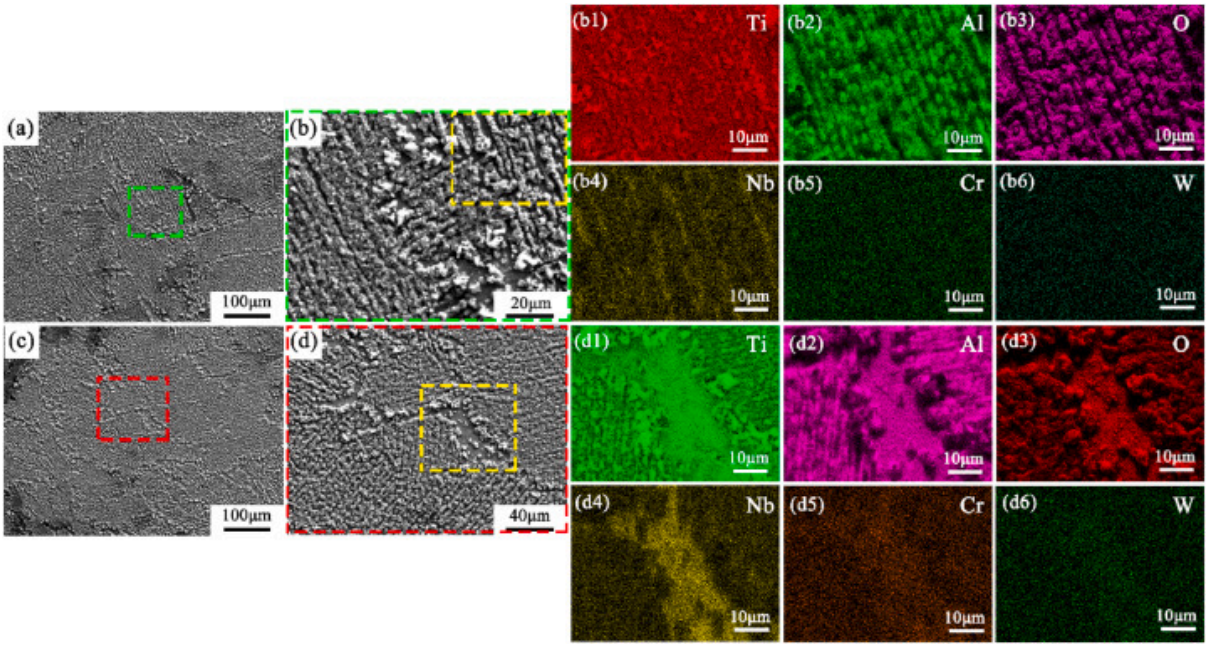


1. Download: Download high-res image (2MB)
2. Download: Download full-size image

Fig. 8. Cross-sectional morphology of the DS high Nb TiAl alloy after oxidation at 800 °C for 100 h: (a) cross-sectional microstructure, (b)~(g) EDS elemental distribution mapping of (a).

3.4.3.2. 850 °C results

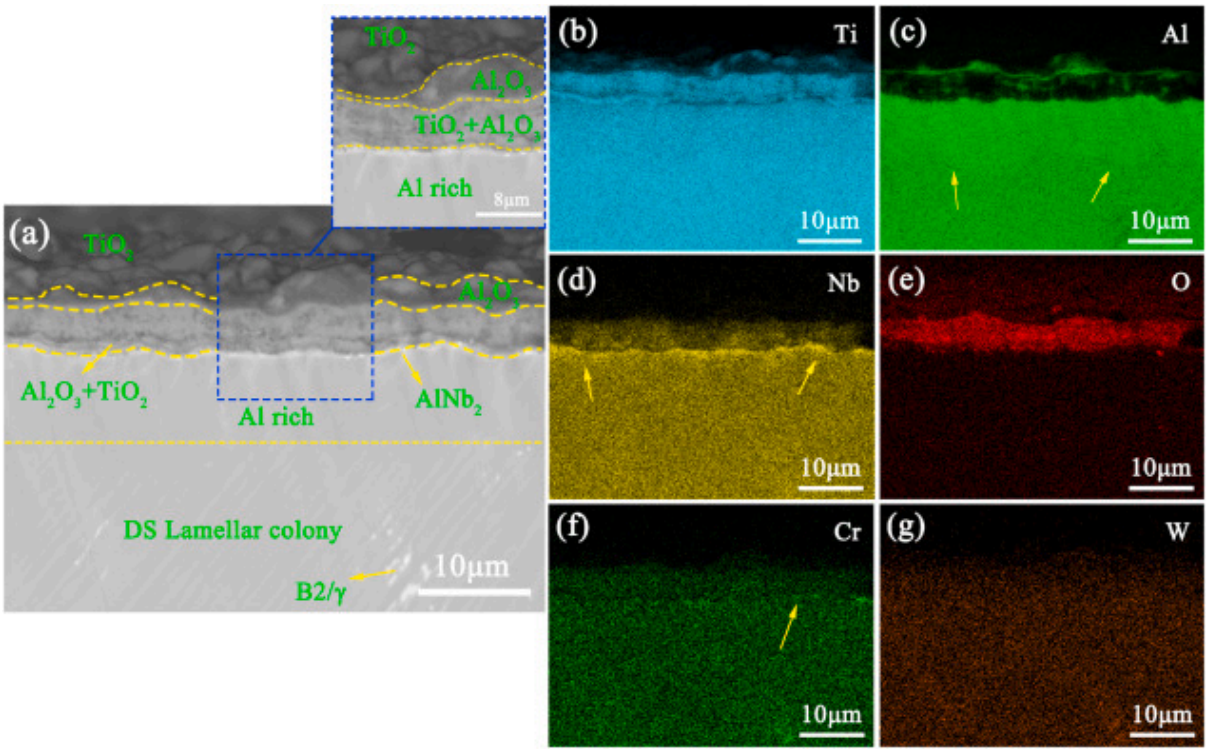
Fig. 9 shows the oxide surface morphology of the DS high Nb TiAl based alloy after 100 h oxidation at 850 °C. Similar observations were noted as those in the 800 °C sample above, with alumina particles with different orientations along the lamellar growth direction. The size of the oxide particles increased significantly compared to the 800 °C sample, there is a higher density of oxide particles. The elemental distribution maps (Fig. 9(b1)-(b6)) show Al and O enrichment along the lamellar direction, while Ti is enriched on the surface of alumina, which indicates TiO_2 diffusion through the Al_2O_3 layer and preferential growth on the surface of the oxide layer at 850 °C or higher temperatures. A Nb enriched zone is observed between the oxide particles, indicating a Nb enriched layer deeper in the oxide layer, as evident in Fig. 9(b4). It can be seen from the EDS results at the junction of the lamellar colony (Fig. 9(d1)-(d6)) that Nb content at the junction is significantly higher than that in other regions; furthermore, there is evidence of slight W and Cr enrichment in this region.



1. Download: Download high-res image (3MB)
2. Download: Download full-size image

Fig. 9. Microscopic oxidation surface morphology of DS high Nb TiAl alloy after oxidation at 850 °C for 100 h, (a)~(b) lamellar colony, (d1)~(d6) elemental EDS mapping of (d), (c) and (d) junction of lamellar colony, (f1)~(f6) elemental EDS mapping of (f).

Fig. 10 shows the oxide cross-sectional morphology of DS high Nb TiAl alloy after 100 h oxidation at 850 °C. As the temperature increases from 800 °C to 850 °C, the oxide layer thickness increases from 2.4 μm to 5.2 μm. Observing the elemental distribution maps in Fig. 10(b)–(g), the top of the sample contains a Ti-rich layer with the Al rich region below this layer, followed by ~3.5 μm thick Ti rich region and, finally a Ti and Al rich oxide layer before the metal matrix. Therefore, the oxidation layer from top to bottom at 850 °C is a TiO_2 layer, an Al_2O_3 layer and a TiO_2+Al_2O_3 layer, respectively. The interface between the oxide layer and the matrix transition zone is rougher, connecting the oxide layer to the matrix. The thickness of the matrix transition zone also increased to 8.4 μm. The depletion of Ti and enrichment of Al in the matrix transition zone is obvious in Fig. 10(b) and (c). Nb accumulated on the surface of the matrix transition zone, while Nb and Cr elements diffused to the oxide layer.

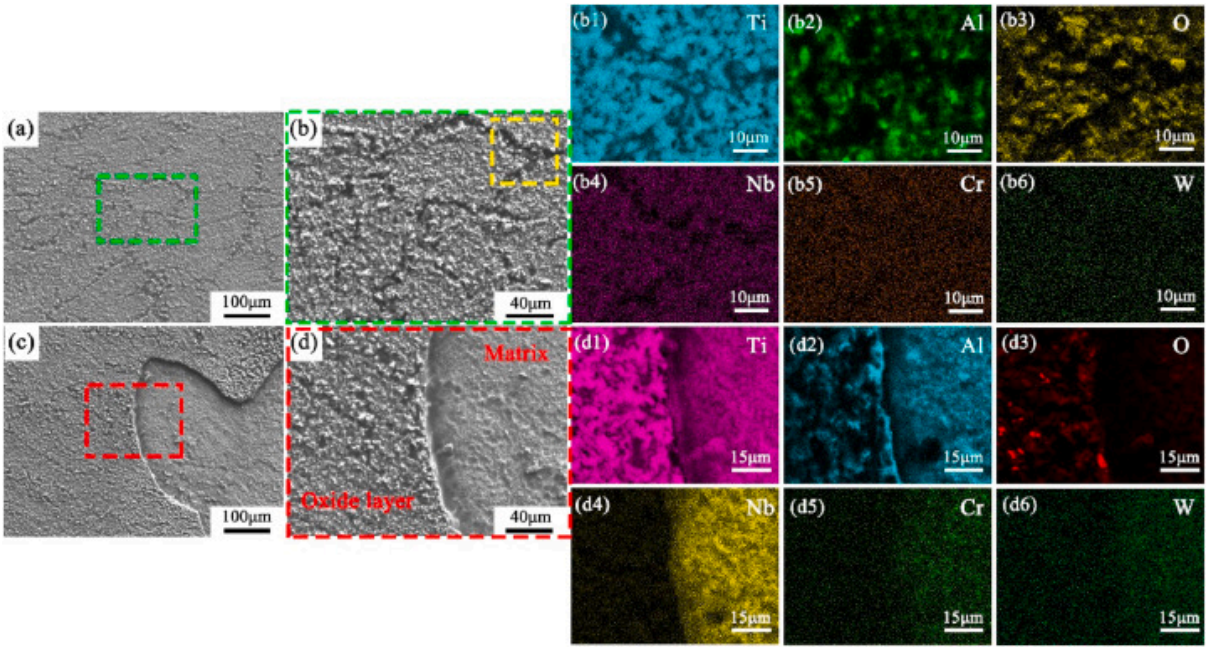


1. Download: Download high-res image (2MB)
2. Download: Download full-size image

Fig. 10. Cross-sectional morphology of the DS high Nb TiAl alloy after oxidation at 850 °C for 100 h: (a) cross-sectional microstructure, (b)~(g) elemental EDS mapping of (a).

3.4.3.3. 900 °C results

When the oxidation temperature is increased to 900 °C (Fig. 11), the oxide particles are closely packed and the oxide size increases significantly. Lamellar colonies with various sizes of are still observed, but the arrangement of the oxides change from along the lamellar direction to a random orientation. This implies that at 900 °C, the two phases in the lamellar colony show insignificant oxidation resistance difference. The surfaces are covered by large oxide regions, there is no obvious difference in lamellar orientation. In addition, the size of the junction of the lamellar colonies is significantly reduced due to an increase in oxide size, as observed in Fig. 11(a) and (b). The distribution of elements is presented in Fig. 11(b1)-(b6) and show Ti enrichment on the surface of the oxide layer and a reduction in Al content as compared with the aforementioned 850 °C sample, indicative of a TiO_2 phase rich surface oxide at this temperature. No enrichment of Nb, W and Cr was observed in the interlamellar region, indicating that the oxide layer was uniform and thick, covering the underlying microstructure. Furthermore, the β-stabilizing elements in the matrix could not be detected.

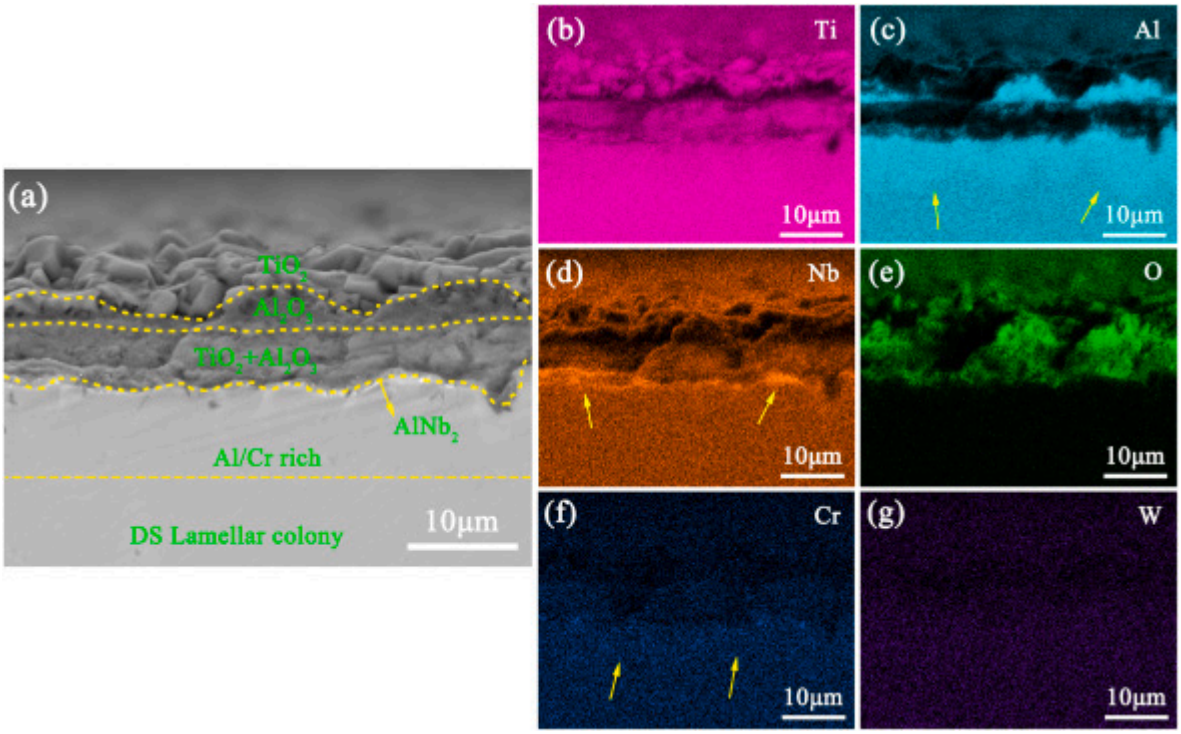


1. Download: Download high-res image (2MB)
2. Download: Download full-size image

Fig. 11. Microscopic oxidation surface morphology of DS high Nb TiAl alloy after oxidation at 900 °C for 100 h, (a)~(b) lamellar colony, (b1)~(b6) elemental EDS mapping of (b), (c) and (d) spalling of the oxide layer, (d1)~(d6) elemental EDS mapping of (d).

Fig. 11(c) and (d) show the surface morphology of oxide layer spalling after oxidation at 900 °C. The left side of the figure is the oxide layer and the right side is the matrix after spalling. After the oxide layer spalls, different sizes of pits appear on the matrix. The existence of such pits is caused by the oxide growing into the matrix. A bonding relationship is formed between the oxide and the matrix, which helps to prevent spalling and improve the oxidation resistance [28]. The corresponding elemental distribution maps for Fig. 11(d) are presented in Fig. 11(d1)-(d6). The surface of the left oxide layer is composed of a large content of TiO_2 phase and a small Al_2O_3 phase content. The matrix on the right showed obvious enrichment of Ti, Al, Nb and Cr, and a slight enrichment of W. This indicates that during oxidation, the elements inside the matrix diffuse to the surface. The accumulation of Nb and W, elements possessing slow diffusion rates on the surface of the matrix, under the oxide layer can reduce elemental diffusion and further oxidation.

After oxidation at 900 °C/100 h (Fig. 12), the oxide layer thickness increases to 11.3 μm. The size of the TiO_2 particles on the outermost surface of the oxide layer grows rapidly, and the stratification of oxide layer is more obvious by virtue of the difference in contrast. Observing Fig. 12(b) and (c), it is seen that the upper layer is Ti rich, followed by an Al rich layer below it. The surface TiO_2 envelopes the internal Al_2O_3 layer. The thickness of the TiO_2 + Al_2O_3 layer under the Al_2O_3 reaches a thickness of 4.6 μm, where the TiO_2 is the main oxide with small amount of Al_2O_3. These two types of oxide phases near the matrix transition zone are intermixed on the transition layer surface which fix the oxide layer to the metal matrix. Compared with the results obtained at 850 °C, the transition layer shows minor growth, increasing in thickness from 8.4 μm at 850 °C to 8.6 μm.



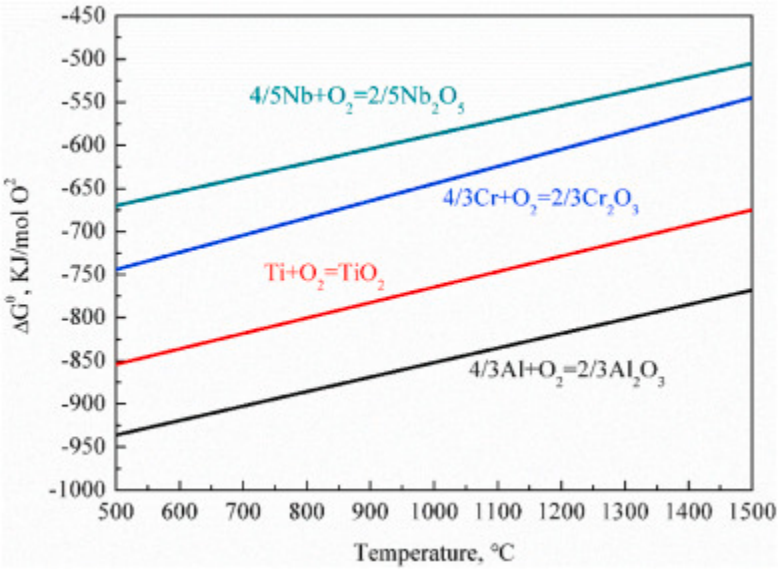
1. Download: Download high-res image (2MB)
2. Download: Download full-size image

Fig. 12. Cross-sectional morphology of the DS high Nb TiAl alloy after oxidation at 900 °C for 100 h: (a) cross-sectional microstructure, (b)~(g) elemental EDS mapping of (a).

4. Discussion

4.1. Thermodynamics and kinetics of oxidation

To explain the mechanism of oxidation observed, we provide the Ellingham diagram of the standard Gibbs free energy for each of the possible oxides in our alloy in Fig. 13. As seen in the diagram, the preference in oxide formation from most to least preferred is as follows; Al_2O_3, TiO_2, Cr_2O_3 and N_2O_5. Al_2O_3 has a tendency to form more easily because it has the most negative Gibbs free energy of the oxides in this alloy, verified by this phase encompassing the most volume when oxidized at 800 °C (Fig. 7). With increasing temperatures, the rapid growth of TiO_2 led to a composite of TiO_2 phase and Al_2O_3 phase in the middle oxide layer and a final TiO_2 phase in the outmost layer (Fig. 10, Fig. 12). It is worth noting that the Nb_2O_5 phase is detected in the XRD results, despite its high Gibbs free energy. Yoshihara et al. [18] studied the effect of Nb on the oxidation behavior of TiAl alloys and found that when the Nb addition is between 1 and 10 at.%, Nb can replace Ti ions in TiO_2, thus forming Nb_2O_5 and inhibiting the growth of TiO_2. In this work, 7 at% Nb is added and is clearly observed to be distributed uniformly in the TiO_2 layer from the elemental distribution maps (Fig. 8, Fig. 10, Fig. 12) taken of the oxidation cross-sectional morphology. Therefore, high at% doping of Nb in a TiAl alloy can inhibit the growth of TiO_2 through the formation of Nb_2O_5 in TiO_2, improving the high temperature oxidation resistance.

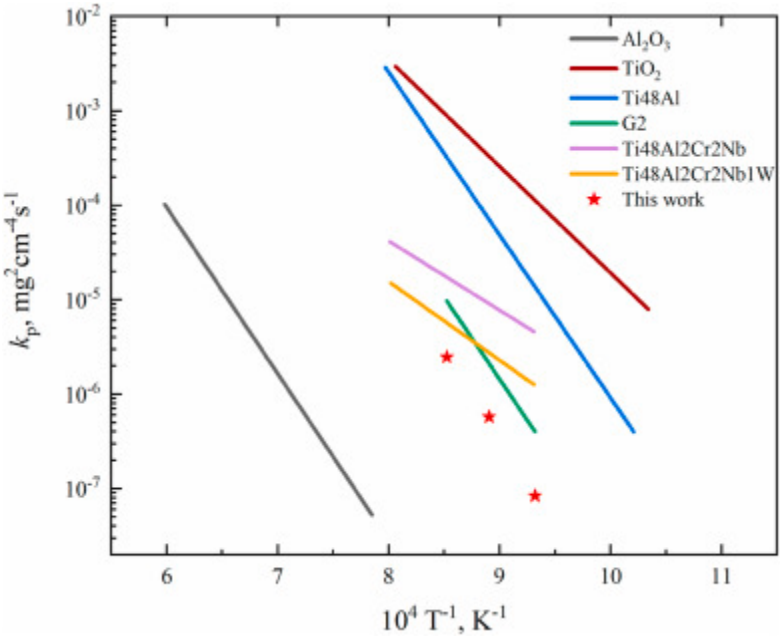


1. Download: Download high-res image (748KB)
2. Download: Download full-size image

Fig. 13. Calculated Ellingham diagram of oxides formed in the high Nb TiAl alloy.

As there was a small amount of Cr added to the alloy, no evidence of Cr_2O_3 phase was detected by XRD or microstructural observations. However, EDS maps show the presence of Cr and W in the TiO_2 layer, suggesting diffusion of these elements into the TiO_2 layer, reducing further inward diffusion of oxygen atoms. Similarly, Shida et al. [41] proposed that the main function of W in TiAl alloys is in the reduction of oxygen solubility, in addition to reducing the defect concentration and the TiO_2 growth rate. Additionally, enrichment of Al on the surface of the matrix transition zone can be observed in the cross-sectional figures (Fig. 8, Fig. 10, Fig. 12). This phenomenon occurs because O diffuses inward and combines with the Ti in the TiAl matrix to form a TiO_2 oxide layer. The oxidation rate of TiO_2 is much higher than that of Al_2O_3, so a large amount of Al will remain in the matrix transition zone. The Al enriched in the transition zone between the oxide layer and the matrix will combine with Nb to form the $AlNb_2$ phase at the interface of the matrix and oxide. The presence of the $AlNb_2$ phase [42] and the possible formation of the Laves phase $(Ti(Cr, Al)_2)$ [21,43] is due to the enrichment of Cr on the surface of the transition zone. The reduced contact between the matrix and the inward diffusion of O and N, prevents further oxidation of the TiAl alloy matrix. With increasing temperature, the volume of $AlNb_2$ and Laves phase on the surface of the matrix transition layer is greater. This not only enhances the protective effect of the matrix, but also results in a rougher interface, strengthening the connection between the oxide layer and the matrix, mitigating oxide layer spalling.

Fig. 14 shows the formation kinetics curve of the DS high Nb TiAl alloy, in comparison with other TiAl alloys and oxides, including Ti-48Al, Ti-48Al-2Cr-2Nb-(0,1)W [23], Ti-(40–45)Al-2Nb-2Mo (G2) [44], TiO_2 and Al_2O_3. It can be found that the k_p values of this and other TiAl alloys are all above the formation range of Al_2O_3 and below that of TiO_2. The oxidation rate of TiO_2 is much higher than that of Al_2O_3, which is also the main reason for its rapid growth with temperature. Importantly, the oxidation rate of the alloy prepared by the DS method is significantly lower than that of other TiAl alloys at the same temperature, indicating that the microalloyed high Nb TiAl alloy has a higher resistance to oxidation. Also, the gradient of the fitted line for this alloy steeper than that of Ti-48Al-2Cr-2Nb-(0,1)W alloys, indicating that the oxidation rate of high Nb TiAl alloy is more sensitive in the 800–900 °C temperature window, with an oxidation rate close to that of the Ti-48Al-2Cr-2Nb alloy at ~1000 °C.

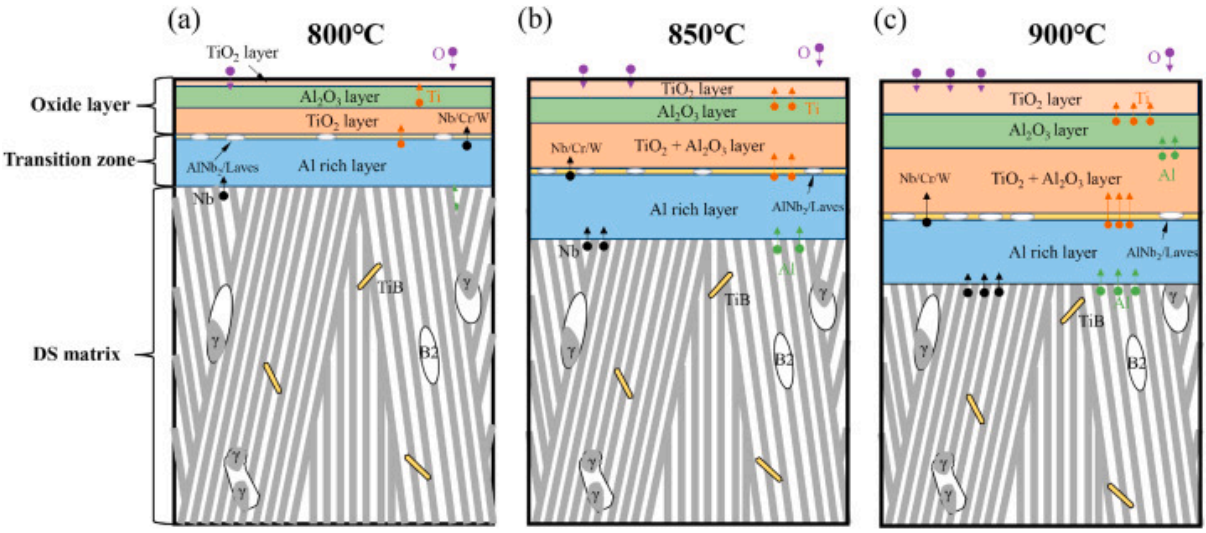


1. Download: Download high-res image (278KB)
2. Download: Download full-size image

Fig. 14. Oxide forming kinetics of the DS microalloyed high Nb TiAl alloy with other TiAl alloys [19,34].

4.2. Formation mechanism of the oxide layer

The schematic diagram presented in Fig. 15 shows the formation mechanism of the oxidation layer of the DS high Nb TiAl alloy. The oxidation behavior of the TiAl alloy containing α_2 and γ phases, consists of three stages: pre-oxidation, selective oxidation of Al and Ti oxide growth [45]. In the pre-oxidation stage, only the oxygen absorption process occurs in the α_2 and the γ phase, with no oxide product formation. Following this stage, selective oxidation produces Al_2O_3, distributed along a specific crystallographic orientation on the TiAl alloy surface. Al_2O_3 formed first due to its relatively lower standard Gibbs free energy, as shown in Fig. 14, Fig. 15 at 800 °C. The diffusion coefficients of the α_2 and the γ phase are $\sim 1 \times 10^{-23}$ and $\sim 1 \times 10^{-21}$ m^2s^{-1}, respectively, which strongly agree with the Al self-diffusion coefficients of the intermetallic phases [[45], [46], [47]], indicating that the growth kinetics are limited by the diffusion of Al to the oxide/metal interface in the alloy. Therefore, due to the different diffusion coefficients of the α_2 and the γ phases, γ phase with the higher Al content show a faster rate of Al_2O_3 formation as compared to the α_2 phase. The oxidation kinetics of α_2 is slower than that of the γ phase, and the thickness of the Al_2O_3 layer in the γ phase is more than that observed in the α_2 phase [45]. Thus, at relatively lower oxidation temperatures the selective oxidation of Al dominates, the γ phase is first oxidized forming Al_2O_3 particles arranged along the γ lamellae inside the α_2/γ lamellar colony. The Al_2O_3 particles on the γ lamellae grow faster and are thicker than those on the α_2 lamellae, which present a parallel arrangement of oxide particles in the lamellar colony. Additionally, adjacent lamellar surfaces show different oxide arrangements, consistent with their lamellar orientations (Fig. 7(a)–(d)).



1. Download: Download high-res image (711KB)
2. Download: Download full-size image

Fig. 15. Schematic diagram depicting the oxidation mechanisms of DS high Nb TiAl alloy at (a) 800 °C, (b) 850 °C and (c) 900 °C.

With increasing oxidation time, simultaneous Ti and Al oxidation occurs. Although Al_2O_3 forms first, TiO_2 will overgrow Al_2O_3 because of its faster growth rate, as seen from the outermost thin TiO_2 layer on the surface (Fig. 15(a)). Meanwhile, O diffuses further inward to form a thick continuous TiO_2 layer with Ti in the matrix. In this layer, Nb, Cr and W are also present by diffusion from the matrix. The TiO_2 layer containing Nb, Cr and W has a higher oxidation resistance than a single TiO_2 layer. Due to the rapid consumption of Ti elements near the matrix an Al-rich transition zone is formed, with the disappearance of the lamellar structure. The $AlNb_2$ phase formed by the enrichment of Al and Nb in this non-lamellar region and the Laves phase formed by the enrichment of Al and Cr on the matrix surface will further prevent the inward diffusion of O.

When the oxidation temperature is increased to 850 °C (Fig. 15(b)), the excessive growth of TiO_2 results in a high content of TiO_2 formed on the outermost layer, gradually breaking through the underlying Al_2O_3 layer. The Al_2O_3 and TiO_2 layer thickness further increased and, an oxide layer with a coexistence of the two oxides is formed in the inner part of the TiO_2 layer. Oxides are arranged along the lamellae due to the different lamellar orientations, the spacing between adjacent oxide particles decreases with increasing oxide particle size. The increase in temperature leads to larger diffusion rate of the elements, including the inward diffusion of O and the outward diffusion of the alloying elements, producing a thicker oxide layer and an intermediate transition zone.

When the oxidation temperature increases to 900 °C (Fig. 15(c)), the surface TiO_2 oxide layer completely covers the Al_2O_3 phase and the oxide layer thickens further. With an increase of the oxide particle size and the thickening of the oxide layer, the sample surface along the lamellar orientation disappears, and a uniform oxide layer will be formed (Fig. 11). Furthermore, the diffusion rate of elements also increases, the faster diffusion rate of O, Ti and Al will lead to an increased thickness of the TiO_2 and the Al_2O_3 layer. The content of $AlNb_2$ and laves phase on the surface of the transition zone increases, but the thickness of the transition layer does not increase further with temperature, which indicates that the increased $AlNb_2$ and laves phases between the matrix and the oxide layer help to reduce the further oxidation of the TiAl alloy.

5. Conclusions

In this paper, a high Nb TiAl alloy with W, Cr and B micro additions was prepared by directional solidification, and its high temperature tensile properties and oxidation behavior were studied at different temperatures. The corresponding oxidation mechanism and oxidation kinetics were elucidated. The main conclusions are summarized as follows.

- (1)

The tensile results show that the ultimate tensile strength of the alloy at 800 °C, 850 °C and 900 °C are 647 MPa, 590 MPa and 508 MPa, respectively. At higher temperatures, the fracture mode changed from brittle cleavage fracture to micro-void accumulation ductile fracture.

- (2)

The microstructure after oxidation includes TiO_2 and Al_2O_3 oxide layers, a non-lamellar transition zone containing a $AlNb_2$ phase and Al/Cr enrichment and an oriented lamellar matrix. At lower temperatures Al_2O_3 forms first, growing along the γ lamellae to form oxide bands aligned with the lamellar orientation. With increasing temperature, the TiO_2 gradually overgrows to the outermost layer and envelopes the Al_2O_3.

- (3)

The oxidation mass gain of the alloy after 900 °C/100 h isothermal oxidation is only 0.91 mg/cm^2. The excellent oxidation resistance is mainly attributed to the formation of a TiO_2 layer containing Nb, Cr and W, an $AlNb_2$ phase and the Al/Cr rich layer above the DS lamellar matrix, which prevents further internal diffusion of oxygen ions.

CRediT authorship contribution statement

Xuesong Xu: Data curation, Formal analysis, Funding acquisition, Investigation, Methodology, Writing – original draft, Writing – review & editing. **He Liang:** Methodology. **Hongsheng Ding:** Funding acquisition, Supervision, Writing – review & editing. **Karl P. Davidson:** Investigation. **R.V. Ramanujan:** Funding acquisition, Supervision, Writing – review & editing. **Ruirun Chen:** Methodology. **Jingjie Guo:** Methodology. **Hengzhi Fu:** Conceptualization.

Data availability

The raw data required to reproduce these findings cannot be shared at this time as the data also forms part of an ongoing study.

Declaration of competing interest

The authors declare that they have no known competing financial interests or personal relationships that could have appeared to influence the work reported in this paper.

Acknowledgements

This work is supported by the National Natural Science Foundation of China under Grant No. 52171112, AME Programmatic Fund by the Agency for Science, Technology and Research, Singapore under Grant No. A18B1b0061, China Scholarship Council, Jiangsu Funding Program for Excellent Postdoctoral Talent and Postdoctoral Fellowship Program of CPSF (GZC20233499). Thanks to Prof. R. Banerjee's help in calculating the phase diagram.

Data availability

No data was used for the research described in the article.

References

1. [1]

R. Swadźba, B. Mendala, L. Swadźba, K. Radwański, L. Sozańska-Jędrasik, A. Pyclik, M. Coppola, S. Barbieri

Corrosion Sci., 227 (2024), Article 111701

View PDFView articleView in ScopusGoogle Scholar

2. [2]

Z. Chen, J. Liu, Y. Wang, T. Ma, D. Zhu, Q. Xing, H. Fang, R. Chen

Ceram. Int., 50 (2024), pp. 2233-2241

View PDFView articleCrossrefGoogle Scholar

3. [3]

P.S.S.R. Krishnan, K.P. Davidson, X. Xu, S.W. Chan, Z. Tsakadze, M. Duchamp, R.V. Ramanujan

J. Mater. Eng. Perform. (2024)

in press

Google Scholar

4. [4]

J. Ding, M. Zhang, Y. Liang, Y. Ren, C. Dong, J. Lin

Acta Mater., 161 (2018), pp. 1-11

View PDFView articleCrossrefGoogle Scholar

5. [5]

L. Yu, X. Song, L. You, Z. Jiao, H. Yu

Scripta Mater., 109 (2015), pp. 61-63

View PDFView articleView in ScopusGoogle Scholar

6. [6]

S.E. Aghili, M. Shamanian, R. Amini

Najafabadi, A. Keshavarzkermani, R. Esmaeilizadeh, U. Ali, E. Marzbanrad, E. Toyserkani

Ceram. Int., 46 (2020), pp. 1668-1679

View PDFView articleView in ScopusGoogle Scholar

7. [7]

S.E. Aghili, M. Shamanian, R. Amini

Najafabadi, H. Ashrafi, E. Marzbanrad, Y. Mahmoodkhani, E. Toyserkani

High temperature corrosion of materials

99 (2023), pp. 311-329

CrossrefView in ScopusGoogle Scholar

8. [8]

T. Sun, Z. Guo, J. Cao, Y. Liang, J. Lin

Corrosion Sci., 213 (2023), Article 110980

View PDFView articleView in ScopusGoogle Scholar

9. [9]

M. Perrut, P. Caron, M. Thomas, A. Couret

C. R. Phys., 19 (2018), pp. 657-671

View PDFView articleCrossrefView in ScopusGoogle Scholar

10. [10]

L. Feng, B. Li, Q. Li, Y. Gao, Z. Pei, C. Liang

Mater. Chem. Phys., 316 (2024), Article 129148

View PDFView articleView in ScopusGoogle Scholar

11. [11]

S. Zhang, N. Tian, D. Li, J. Li, F. Jin, G. Wang, S. Tian

Mater. Sci. Eng. A, 831 (2022), Article 142094

View PDFView articleView in ScopusGoogle Scholar
12. [12]
X. Liu, L. Song, A. Stark, U. Lorenz, Z. He, J. Lin, F. Pyczak, T. Zhang
J. Mater. Sci. Technol., 102 (2022), pp. 89-96
View PDFView articleGoogle Scholar
13. [13]
Y. Ma, J. Yang, Z. Liu, R. Chen
Mater. Sci. Eng. A, 915 (2024), Article 147267
View PDFView articleView in ScopusGoogle Scholar
14. [14]
B. Zhu, X. Xue, H. Kou, X. Li, J. Li
Mater. Sci. Eng. A, 729 (2018), pp. 86-93
View PDFView articleView in ScopusGoogle Scholar
15. [15]
M. Sakaguchi, Y. Niwa, W. Gong, K. Suzuki, H. Inoue
Mater. Sci. Eng. A, 806 (2021), p. 140802
View PDFView articleView in ScopusGoogle Scholar
16. [16]
K. Hashimoto, S. Kajiwara, T. Kikuchi, M. Nakamura
Scripta Metall. Mater., 32 (1995), pp. 417-422
View PDFView articleView in ScopusGoogle Scholar
17. [17]
Y. Wang, X. Liu, D. Dong, D. Zhu, H. Ding, R. Chen, J. Guo, H. Fu
J. Mater. Res. Technol., 25 (2023), pp. 570-580
View PDFView articleView in ScopusGoogle Scholar
18. [18]
M. Yoshihara, K. Miura
Intermetallics, 3 (1995), pp. 357-363
View PDFView articleView in ScopusGoogle Scholar
19. [19]
H. Jiang, M. Hirohasi, Y. Lu, H. Imanari
Scripta Mater, 46 (2002), pp. 639-643
View PDFView articleView in ScopusGoogle Scholar
20. [20]
J.P. Lin, L.L. Zhao, G.Y. Li, L.Q. Zhang, X.P. Song, F. Ye, G.L. Chen
Intermetallics, 19 (2011), pp. 131-136
View PDFView articleView in ScopusGoogle Scholar
21. [21]
M.P. Brady, J.L. Smialek, J. Smith, D.L. Humphrey
Acta Mater., 45 (1997), pp. 2357-2369
View PDFView articleView in ScopusGoogle Scholar
22. [22]
H. Anada, Y. Shida
Mater. Trans., JIM

36 (1995), pp. 533-539
CrossrefView in ScopusGoogle Scholar
23. [23]
D.Y. Seo, T.D. Nguyen, D.B. Lee
Oxid. Metals, 74 (2010), pp. 145-156
CrossrefView in ScopusGoogle Scholar
24. [24]
Z. Gao, R. Hu, H. Zou, M. Zhou, X. Luo
Mater. Des., 241 (2024), Article 112941
View PDFView articleView in ScopusGoogle Scholar
25. [25]
Y. Wu, S.K. Hwang
Acta Mater., 50 (2002), pp. 1479-1493
View PDFView articleView in ScopusGoogle Scholar
26. [26]
J.S. Wu, L.T. Zhang, F. Wang, K. Jiang, G.H. Qiu
Intermetallics, 8 (2000), pp. 19-28
View PDFView articleView in ScopusGoogle Scholar
27. [27]
Y. Pan, X. Lu, M.D. Hayat, F. Yang, C. Liu, Y. Li, X. Li, W. Xu, X. Qu, P. Cao
Corrosion Sci., 166 (2020), Article 108449
View PDFView articleView in ScopusGoogle Scholar
28. [28]
D. Li, G. Zhang, G. Lu, J. Wang, C. Liu
Corrosion Sci., 177 (2020), Article 108971
View PDFView articleView in ScopusGoogle Scholar
29. [29]
G. Chen, Z. Sun, X. Zhou
Corrosion, 48 (1992), pp. 939-946
CrossrefView in ScopusGoogle Scholar
30. [30]
S.K. Varma, A. Chan, B.N. Mahapatra
Oxid. Metals, 55 (2001), pp. 423-435
View in ScopusGoogle Scholar
31. [31]
L. Mengis, A.S. Ulrich, P. Watermeyer, C.H. Liebscher, M.C. Galetz
Corrosion Sci., 178 (2021), Article 109085
View PDFView articleView in ScopusGoogle Scholar
32. [32]
S. Taniguchi, T. Shibata, S. Itoh
Mater. Trans., JIM, 32 (1991), pp. 151-156
CrossrefView in ScopusGoogle Scholar
33. [33]
Y. Wang, C. Liu, T. Ma, Y. Liu, Y. Zhang, L. Zhou

Corrosion Sci., 208 (2022), Article 110639
View PDFView articleView in ScopusGoogle Scholar
34. [34]
X. Xu, H. Ding, H. Huang, H. Liang, R. Chen, J. Guo, H. Fu
J. Mater. Res. Technol., 11 (2021), pp. 2221-2234
View PDFView articleView in ScopusGoogle Scholar
35. [35]
X. Xu, H. Ding, H. Huang, H. Liang, H. Guo, R. Chen, J. Guo, H. Fu
J. Mater. Sci. Technol., 127 (2022), pp. 115-123
View PDFView articleView in ScopusGoogle Scholar
36. [36]
X. Xu, H. Ding, H. Huang, H. Liang, R.V. Ramanujan, R. Chen, J. Guo, H. Fu
Int. J. Fatig. (2023), Article 107597
View PDFView articleView in ScopusGoogle Scholar
37. [37]
M. Li, S. Xiao, Y. Chen, L. Xu, J. Tian
J. Alloys Compd., 775 (2019), pp. 441-448
View PDFView articleView in ScopusGoogle Scholar
38. [38]
G. Zheng, B. Tang, S. Zhao, W.Y. Wang, X. Chen, L. Zhu, J. Li
Acta Mater., 225 (2022), Article 117585
View PDFView articleView in ScopusGoogle Scholar
39. [39]
Z. Liang, S. Xiao, H. Yue, X. Li, Q. Li, Y. Zheng, L. Xu, X. Xue, J. Tian, Y. Chen
Corrosion Sci., 220 (2023), Article 111287
View PDFView articleView in ScopusGoogle Scholar
40. [40]
E.U. Lee, J. Waldman
Scripta Metall., 22 (1988), pp. 1389-1394
View PDFView articleView in ScopusGoogle Scholar
41. [41]
Y. Shida, H. Anada
Corrosion Sci., 35 (1993), pp. 945-953
View PDFView articleView in ScopusGoogle Scholar
42. [42]
W. Lu, C.L. Chen, L.L. He, F.H. Wang, J.P. Lin, G.L. Chen
Corrosion Sci., 50 (2008), pp. 978-988
View PDFView articleView in ScopusGoogle Scholar
43. [43]
S.J. Qu, S.Q. Tang, A.H. Feng, C. Feng, J. Shen, D.L. Chen
Acta Mater., 148 (2018), pp. 300-310
View PDFView articleView in ScopusGoogle Scholar
44. [44]
D.J. Kim, D.Y. Seo, H. Saari, T. Sawatzky, Y.W. Kim

Intermetallics, 19 (2011), pp. 1509-1516
View PDFView articleView in ScopusGoogle Scholar
45. [45]
V. Maurice, G. Despert, S. Zanna, P. Josso, M.P. Bacos, P. Marcus
Acta Mater., 55 (2007), pp. 3315-3325
View PDFView articleView in ScopusGoogle Scholar
46. [46]
Y. Mishin, C. Herzig
Acta Mater., 48 (2000), pp. 589-623
View PDFView articleView in ScopusGoogle Scholar
47. [47]
M.W. Brumm, H.J. Grabke
Corrosion Sci., 33 (1992), pp. 1677-1690
View PDFView articleView in ScopusGoogle Scholar